JCI The Journal of Clinical Investigation

Suppression of the SLC7A11/glutathione axis causes synthetic lethality in *KRAS*-mutant lung adenocarcinoma

Kewen Hu, … , Mingyao Liu, Xiufeng Pang

J Clin Invest. 2019. https://doi.org/10.1172/JCI124049.

Research In-Press Preview Oncology

Graphical abstract

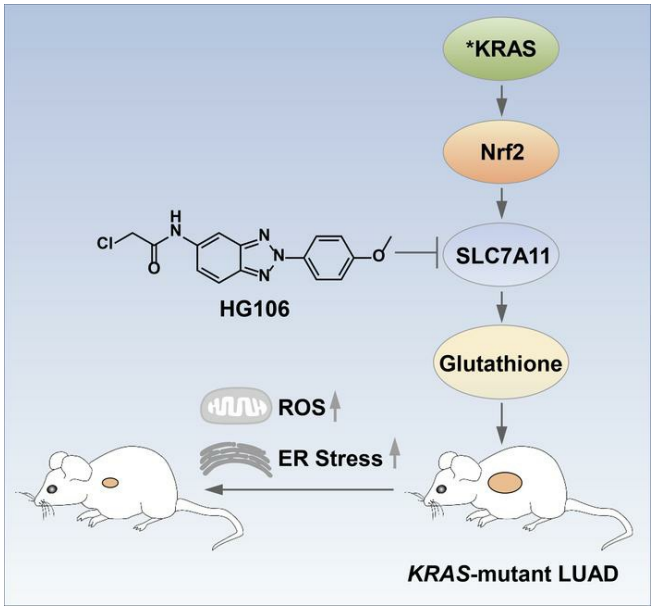

Suppression of the SLC7A11/glutathione axis causes synthetic lethality in *KRAS*-mutant lung adenocarcinoma

Kewen Hu[1,2], Kun Li[1], Jing Lv[1], Jie Feng[3], Jing Chen[4], Haigang Wu[1], Feixiong Cheng[5,6,7], Wenhao Jiang[1], Jieqiong Wang[2], Haixiang Pei[1], Paul J. Chiao[8], Zhenyu Cai[9], Yihua Chen[1], Mingyao Liu[1,10] and Xiufeng Pang[1]

[1] Shanghai Key Laboratory of Regulatory Biology, Institute of Biomedical Sciences and School of Life Sciences, East China Normal University, Shanghai 200241, China; [2]Cancer Institute, Fudan University Shanghai Cancer Center, Department of Oncology, Shanghai Medical College, Fudan University, Shanghai 200032, China; [3] Beijing neurosurgical institute, Beijing Tiantan Hospital, Capital Medical University, Beijing 100050, China; [4] Key Laboratory of Reproduction and Genetics in Ningxia, Ningxia Medical University, Yinchuan 750004, China; [5] Genomic Medicine Institute, Lerner Research Institute, Cleveland Clinic, 9500 Euclid Avenue, Cleveland, OH 44195, USA; [6] Department of Molecular Medicine, Cleveland Clinic Lerner College of Medicine, Case Western Reserve University, Cleveland, OH 44195, USA; [7] Case Comprehensive Cancer Center, Case Western Reserve University School of Medicine, Cleveland, Ohio 44106, USA; [8] Department of Molecular and Cellular Oncology, The University of Texas MD Anderson Cancer Center, Houston, Texas 77030, USA; [9] National Center for Liver Cancer, Eastern Hepatobiliary Surgery Hospital, Second Military Medical University, Shanghai 200433, China; [10] Institute of Biosciences and Technology, Department of Molecular and Cellular Medicine, Texas A&M University Health Science Center, Houston, Texas 77030, USA.

Running title: Targeting metabolic synthetic lethality to defeat *KRAS*-mutant LUAD.

Keywords: KRAS, glutathione biosynthesis, SLC7A11, synthetic lethality, lung adenocarcinoma

Author note: KH, KL and JL are co-first authors. YC, ML and XP are co-corresponding authors.

To whom correspondence should be addressed:
Dr. Xiufeng Pang
Institute of Biomedical Sciences and School of Life Sciences
East China Normal University
500 Dongchuan Rd.
Shanghai 200241, China

Office phone: +86-21-24206942
Office fax: +86-21-54344922
E-mail: xfpang@bio.ecnu.edu.cn

Dr. Mingyao Liu
Institute of Biosciences and Technology
Texas A&M University Health Science Center
2121 W. Holcombe Blvd.
Houston, TX 77030
Office phone: 713-677-7505
Office fax: 713-677-7512
E-mail: mliu@ibt.tamhsc.edu

Dr. Yihua Chen
Institute of Biomedical Sciences and School of Life Sciences
East China Normal University
500 Dongchuan Rd.
Shanghai 200241, China
Office phone: +86-21-24206647
Office fax: +86-21-54344922
E-mail: yhchen@bio.ecnu.edu.cn

Conflicts of Interest: The authors have declared that no conflict of interest exists.

Abstract

Oncogenic KRAS is a major driver in lung adenocarcinoma (LUAD) that has yet to be therapeutically conquered. Here we report that the SLC7A11/glutathione axis displays metabolic synthetic lethality with oncogenic KRAS. Through metabolomics approaches, we found that mutationally activated KRAS strikingly increased the intracellular cystine level and glutathione biosynthesis. SLC7A11, a cystine/glutamate antiporter conferring specificity for cystine uptake, was overexpressed in patients with *KRAS*-mutant LUAD and showed positive association with tumor progression. Furthermore, SLC7A11 inhibition either by genetic depletion or pharmacological inhibition by sulfasalazine resulted in selective killing across a panel of *KRAS*-mutant cancer cells in vitro and tumor growth inhibition in vivo, suggesting the functionality and specificity of SLC7A11 as a therapeutic target. Importantly, we further identified a potent SLC7A11 inhibitor, HG106 that markedly decreased cystine uptake and intracellular glutathione biosynthesis. Furthermore, HG106 exhibited selective cytotoxicity towards *KRAS*-mutant cells by increasing oxidative stress- and endoplasmic reticulum stress-mediated cell apoptosis. Of note, treatment of *KRAS*-mutant LUAD with HG106 in several lung cancer preclinical mouse models led to marked tumor suppression and prolonged mouse survival. Overall, our findings reveal that *KRAS*-mutant LUAD cells are vulnerable to SLC7A11 inhibition, providing promising therapeutic approaches to the treatment of this currently incurable disease.

Introduction

Lung cancer is the leading cause of global cancer-related mortality, and lung adenocarcinoma (LUAD) represents the most common histological subtype of this disease. Approximately two-thirds of LUADs have activated oncogenes, such as *EGFR, KRAS*, translocated *ALK*, *RET* or *ROS1.* Among them, mutations in *KRAS* occur in nearly 30% of all lung cancer cases. Oncogenic KRAS mutations frequently compromise its GTPase activity, locking the protein in a persistent GTP-bound state and activating downstream signaling pathways, ultimately initiating lethal malignancies, including LUAD (1). Molecular targeted therapies have significantly improved the survival of patients with a therapeutically targetable lesion compared with conventional chemotherapy (2, 3). However, no therapeutic agent directly targeting RAS has been clinically approved (4, 5). Strategies to inhibit KRAS have been hindered by the lack of a proper binding pocket for small molecules. Recently, an atropisomeric inhibitor directly targeting mutant KRAS(G12C), a specific mutation in 11%-16% of LUAD, has been reported to achieve benefits in mice and in clinical trials (6-9). However, its action in patients still needs to be determined. Strategies to target KRAS downstream effectors showed modest or no clinical responses in *KRAS*-mutant LUAD either through single agents or in combination with chemotherapy (10-12). This can be explained by the reactivation of upstream kinases, alternative pathway effectors, KRAS dimerization or other intrinsic and adaptive resistance mechanisms (10, 13). Therefore, the need to develop alternative options for *KRAS*-mutant LUAD is still imperative.

KRAS mutations are frequently associated with a metabolic reprogramming, such as highly active glucose metabolism, differential channeling of glucose intermediates, reprogrammed glutamine metabolism, increased autophagy and macropinocytosis (4, 14). These changes are critical for utilization of nutrients to satisfy biosynthetic demands and maintain redox equilibrium for cell survival. In order to support their growth, cells harboring *KRAS* mutations may undergo oncogenic stress to which cancer cells have to adapt. As a result, *KRAS*-mutant cancers become highly dependent on their metabolic adaptations, thereby exposing their Achilles' heel (15, 16). In cancer cells overexpressing specific oncogenes that are difficult to target directly, such as mutant KRAS, silencing their synthetic lethal partners would lead to specific elimination of these cells without harming normal cells. Emerging evidence implies that *KRAS*-mutant cancers are vulnerable to inhibition of their aberrant metabolism, and metabolic synthetic lethality can be an ideal target (17, 18).

In this study, we investigated metabolic networks in paired KRAS wild-type and mutant isogenic cells through metabolomics analysis, aiming to unravel metabolic vulnerabilities for the treatment of *KRAS*-mutant LUAD. This work identified solute carrier family 7 member 11 (SLC7A11; also known as xCT) as a protein with altered expression upon KRAS mutation, resulting in rewiring glutathione metabolism. SLC7A11 is the

functional light chain subunit of the cystine/glutamate antiporter system xc(-), and confers specificity for cystine uptake, a major rate-limiting factor in glutathione biosynthesis (19). SLC7A11 is overexpressed in several cancer types, including glioma, liver carcinoma, non-small cell lung cancer, and triple-negative breast cancer, and serves as an independent prognostic factor (20-24). SLC7A11 also contributes to glutathione-based drug resistance (25-27). However, the specific role and therapeutic implications of SLC7A11 induction in *KRAS*-mutant LUAD remain elusive. Here we systemically investigated the synthetic lethal role of SLC7A11 in *KRAS*-transformed cells in vitro and in vivo. By chemical screening, we further identified HG106, a molecule with a new structure, as a potent SLC7A11 inhibitor. Inhibition of SLC7A11 by HG106 led to enhanced reactive oxygen species generation, endoplasmic reticulum stress and ultimately growth arrest specifically in *KRAS*-mutant LUAD.

Results

Mutant KRAS drives reprogramming of glutathione metabolism.

To explore metabolic vulnerability in cancer cells driven by *KRAS* mutations, we obtained isogenic human pancreatic epithelial nestin-expressing (HPNE) cells with or without expression of constitutively active mutant KRAS(G12V) (28). We performed gas chromatography with time-of-flight mass spectrometry (GC/TOF-MS)-based metabolomics analysis. Hierarchical clustering and heatmap analysis revealed that HPNE and HPNE/KRAS were grouped into distinct metabolite clusters, implying a marked difference in their metabolic signatures (Figure 1A and Supplementary Table 1). The pathway enrichment of those significantly changed metabolites further demonstrated that many metabolic pathways were increased in *KRAS*-mutant cells, with the glutathione metabolism pathway most significantly affected (Figure 1B and Supplementary Table 2). Although arginine and proline metabolism pathway was enriched comparably to glutathione metabolism in our experimental system, we could not deduce any mechanistic explanation for the role of arginine and proline metabolism in *KRAS*-mutant lung cancer from the existing literatures. Since glutathione metabolism has shown an emerging role in the growth of *KRAS*-driven cancers (29-32), we thus concentrated on this metabolic pathway for the mechanism study and inhibitor identification. As indicated in Figure 1C, the critical intermediates of glutathione metabolism in HPNE/KRAS cells were significantly upregulated, including cystine, glutamate and glutathione. Cystine, a major rate-limiting factor in the process of glutathione biosynthesis, is imported by the cystine/glutamate antiporter system xc(-) from extracellular environment. Hence, we quantified cystine levels in two paired isogenic cell lines that were selected based on the dependence of growth and viability on mutant KRAS status. As expected, both *KRAS*-mutant HPNE (HPNE/KRAS) and H522 (H522/KRAS) cells exhibited much higher levels of Na^+-independent [^{14}C]-cystine uptake (Figure 1D, *left*), accompanied by a remarkable increase in glutathione biosynthesis compared to their wild-type counterparts (Figure 1D, *middle*). As a consequence of glutathione upregulation, *KRAS*-mutant cells generated a higher ROS level to maintain redox equilibrium (Figure 1D, *right*). This is in accord with previous studies that abundant ROS production is one of the characteristics of RAS activation (31, 33). These data collectively suggest that *KRAS*-mutant cells sustain highly active glutathione biosynthesis by absorbing more cystine from the extracellular environment.

SLC7A11 is overexpressed in *KRAS*-mutant LUAD.

Given that *KRAS*-mutant cells uptake more cystine, we set out to determine whether SLC7A11, a specific and functional subunit of system xc(-), is the dominant factor of this biological process. By using paired KRAS isogenic lung and pancreatic cell lines, we found that mutant KRAS upregulated SLC7A11 mRNA level (Figure 2A). The

transcription level of NF-E2-related factor 2 (Nrf2; encoded by *NRF2*, also known as *NFE2L2*), a specific transcription factor of SLC7A11 (34), was coincidently upregulated in HPNE/KRAS and H522/KRAS cells (Figure 2A). Moreover, the protein abundance of SLC7A11 and Nrf2 were elevated by introduction of KRAS mutations (Figure 2B). To further support these findings, we additionally examined SLC7A11 protein expression in mouse lung tumors. Our Western blot analysis (Figure 2C) showed that there was an obvious increase of SLC7A11 expression in lung tumor tissue compared to adjacent normal tissue in LSL-$Kras^{G12D}$ transgenic mice 4 months after induction by intra-tracheal delivery of adenovirus-Cre. Similar results were additionally observed in isolated mouse embryonic fibroblasts cells (Figure 2D). These data demonstrate a positive relationship of SLC7A11 expression with KRAS mutational status. To investigate the mechanism of Nrf2 regulation by oncogenic KRAS, we silenced KRAS in *KRAS*-mutant A549 and H441 cells, and we found that Nrf2 and SLC7A11 protein levels were coincidently decreased (Figure 2E), implying that Nrf2 might be a target of KRAS. To understand the mechanisms of SCL7A11 upregulation by Nrf2, we generated Nrf2 knockout A549 and H441 cell lines via CRISPR/Cas9. Our results showed that genetic disruption of Nrf2 led to obvious SLC7A11 suppression (Figure 2F), implying that Nrf2 mediated SLC7A11 expression in the setting of KRAS mutations. To identify KRAS effectors responsible for Nrf2 and SLC7A11 expression, we further used several pharmacological inhibitors to specifically block the main downstream pathways of KRAS including the MAPK pathway, the PI3K-AKT pathway and the Ral pathway, in A549 (Figure 2, G-H) and H441 cells (Supplementary Figure 1, A-B). Our results showed that blockade of the key components downstream of KRAS decreased SLC7A11 and Nrf2 expression at both mRNA and protein levels. These results suggest that key pathways downstream of KRAS share the ability to modulate the Nrf2/SLC7A11 axis, implying a cooperative regulatory mechanism.

In parallel, we investigated clinical implications of SLC7A11 in patients with lung adenocarcinoma harboring *KRAS* mutations. We collected primary lung adenocarcinoma samples (*n*=51) from the General Hospital of Ningxia Medical University, Ningxia, China. Tumor samples of patients were further categorized based on *KRAS* mutational status analyzed by direct DNA sequencing. Immunohistochemical analysis showed that SLC7A11 expression was higher in LUAD compared with adjacent normal lung tissues (Figure 2I). Our bioinformatics analysis (Supplementary Figure 2A), together with other observations (22-24), showed that SLC7A11 was overexpressed in several human cancer types. Importantly, when classifying LUAD samples into *KRAS*-mutant and wild-type groups, we strikingly found that *KRAS*-mutant LUAD possessed much higher abundance of SLC7A11 compared to *KRAS* wild-type ones (Figure 2J). Furthermore, the increased protein level of SLC7A11 was significantly associated with tumor progression as indicated by T staging (Figure 2K). Of note, the elevated *SLC7A11* gene expression

was correlated with the *KRAS* and *NRF2* expression levels in TCGA datasets of human LUAD (*n*=93; Supplementary Figure 2B). These results collectively suggest that SLC7A11 is overexpressed in *KRAS*-mutant LUAD and potentially involved in tumor progression in patients.

As the Keap1/Nrf2 pathway often alters in LUAD and squamous-cell carcinoma of the lung, we next examined the Keap1 expression in paired KRAS isogenic pancreatic and lung cell lines (HPNE and HPNE/KRAS; H522 and H522/KRAS). By contrast to elevated Nrf2 expression (Figure 2, A-B), the Keap1 levels were little changed in these cell pairs (Supplementary Figure 3). To further query the correlations between SLC7A11 and Nrf2 or Keap1 status, we performed immunohistochemical staining to assess the Nrf2 and Keap1 expression levels in human lung adenocarcinoma (Supplementary Figure 4, A-B). Our results showed that Nrf2 was overexpressed in human *KRAS*-mutant LUAD compared with its levels in *KRAS* wild-type LUAD or adjacent normal lung tissue. Furthermore, high Nrf2 expression was correlated with high SLC7A11 expression in *KRAS*-mutant LUAD (Supplementary Figure 4C). However, by contrast, the Keap1 IHC signal did not differ among these groups, and did not show correlation with SLC7A11 expression (Supplementary Figure 4B and 4D), indicating that activation of Nrf2 and SLC7A11 might occur via Keap1 independent mechanisms.

Silencing SLC7A11 selectively kills *KRAS*-mutant LUAD cells.

To explore the functional role of SLC7A11 in cell growth, we depleted SLC7A11 in those KRAS isogenic cell lines (Figure 3A, *left*). The specificity of the targeting of the small interfering RNAs to SLC7A11 was tested by using C911 oligonucleotides (Supplementary Figure 5). Our results showed that silencing SLC7A11 suppressed cell growth (Figure 3A, *middle* and *right*) and promoted ROS production with high selectivity towards *KRAS*-mutant cells, leaving their wild-type counterparts little affected (Figure 3B). Based on these observations, we further tested sensitivity to SLC7A11 depletion across an additional 32 cancer cell lines (Supplementary Table 3). Our results showed that SLC7A11 depletion led to a significant difference in toxicity between *KRAS*-mutant and wild-type cell lines (Figure 3C). In attempting to validate SLC7A11 as a mutant KRAS-associated vulnerability, we tested the effects of SLC7A11 inhibitor sulfasalazine in KRAS experimental systems. Sulfasalazine, an FDA-approved drug, is typically used to treat chronic inflammatory disease and has been shown to decrease the supply of cystine (35). In our paired KRAS isogenic cell lines, we found that *KRAS*-mutant cells were more vulnerable to sulfasalazine treatment and exhibited much lower IC_{50} values (Figure 3D). In agreement, sulfasalazine selectively killed *KRAS*-mutant cancer cell lines compared to *KRAS* wild-type ones, with much lower IC_{50}s (Figure 3E). Sulfasalazine also remarkably reduced the growth of A549 in long-term clonogenic assays (Figure 3F) and anchorage-independent growth assays (Figure 3G). These results indicate the

selectivity and potency of SLC7A11 inhibition towards *KRAS*-mutant LUAD cells.

Sulfasalazine leads to tumor regression in vivo.

In light of the above in vitro findings, we further tested the therapeutic effect of sulfasalazine in the LSL-Kras^{G12D} mouse model in vivo. After oncogene expression was induced by adenovirus expressing Cre recombinase for 12 weeks, mice were randomly treated with vehicle, trametinib or sulfasalazine for an additional 4 weeks (Figure 4A). When compared with the vehicle group, addition of sulfasalazine at a dose of 250 mg/kg daily schedule led to a marked tumor inhibition (Figure 4, B-C) and produced a significant improvement in overall survival (Figure 4D). The efficacy exerted by sulfasalazine was comparable to that of the MEK inhibitor trametinib at a dosage of 1 mg/kg/d. Taken together, these results suggest that SLC7A11 is essential for the growth of *KRAS*-mutant LUAD in vivo, and targeting SLC7A11 represents a potential therapeutic strategy for the treatment of this incurable disease.

Identification of HG106 as a potent SLC7A11 inhibitor.

Sulfasalazine exhibited selective inhibition of *KRAS*-mutant lung cancer cells while sparing wild-type counterparts (Figure 3 and Figure 4). However, all current available SLC7A11 inhibitors, including sulfasalazine, displayed low target specificity against SLC7A11 (19). This was also evidenced by our in vivo data that sulfasalazine produced satisfactory therapeutic efficacy only at high dosages as much as 250 mg/kg daily (Figure 4, B-C). High-dosage administration of sulfasalazine probably will result in adverse and off-target effects when used for the treatment of human cancers. Hence, we sought to identify more potent inhibitors of SLC7A11 by screening compounds while monitoring cellular cystine uptake and glutathione biosynthesis through radioactivity and fluorescence, respectively.

A primary screening was carried out on a commercial library based on their inhibitory effects on glutathione production in A549 cells. The mean value and standard deviation of the experimental population screened were expressed as Z_{Scores}. Because the Z_{Score} indexes of the majority of the compounds ranged from 2 to −2, we considered “hits” with Z_{Scores} lower than -3. Based on this cut-off, we identified 8 compounds that potently decreased glutathione production, with compound 575148 ranking at the top (Supplementary Figure 6A). Intriguingly, most of these effective compounds belonged to a series of chemicals with a benzotriazole scaffold. Therefore, several derivatives were further synthesized and modified based on the structure properties of compound 575148 (Supplementary Table 4). Those derivatives were subsequently evaluated in a subscreen on cellular glutathione level and cystine uptake. The effects of synthesized derivatives on glutathione production and [^{14}C]-cystine consumption were shown in Supplementary Figure 6B. The small-molecule HG106 (Figure 5A) exhibited best

potency and efficacy, and was thereby selected as a candidate for further evaluation against KRAS-mutant LUAD. HG106 inhibited [^{14}C]-cystine consumption (Figure 5B) and glutathione production (Figure 5C) in a concentration-dependent manner in KRAS-mutant LUAD cells, with an effective concentration starting at 1.25 μmol/L. The efficacy of HG106 at 10 μmol/L was comparable to that of sulfasalazine at a concentration of 1 mmol/L, indicating a 100-fold increase in activity of HG106.

In attempting to confirm and validate the on-target specificity of HG106, we next performed metabolomic profiling to characterize metabolic changes mediated by HG106 treatment. Our results showed that HG106 rewired multiple metabolic pathways, and as expected, glutathione biosynthesis ranked at the top (Figure 5D, Supplementary Table 5 and Supplementary Table 6). The levels of key metabolites in the glutathione metabolism pathway, such as cystine, glutathione and glycine, were all suppressed (Figure 5E and Supplementary Table 7). HG106 exerted substantial cytotoxic effects on *KRAS*-mutant H441 and A549 cells, whereas this could be strikingly reduced by addition of β-mercaptoethanol and L-cysteine (Figure 5F), as they were reported to active GSH synthesis through a direct increase in cysteine transport (36, 37). Moreover, genetic depletion of SLC7A11 significantly reduced the potency of HG106, suggesting its specificity towards SLC7A11 (Figure 5G). Similar results were also observed in A549 cells harboring a G12S mutation in *KRAS* (Supplementary Figure 7, A-B). HG106 activated ERK, whereas it exhibited no obvious inhibitory actions on a panel of kinases (Supplementary Table 8), the RAS activity and other MAPK pathway components (Supplementary Figure 8).

HG106 preferentially decreases the viability of *KRAS*-mutant LUAD cells.

SLC7A11 promotes cystine uptake and glutathione biosynthesis, leading to protection from oxidative stress (19). We thereby hypothesized that SLC7A11 inhibition by HG106 would lead to increased ROS in *KRAS*-mutant cells. We performed flow cytometry to measure ROS levels. As shown in Figure 6A, HG106 dose-dependently increased total ROS levels in A549 cells. Treatment with the ROS scavenger N-acetyl-cysteine significantly reduced the cytotoxicity of HG106 (Figure 6B), supporting a role of ROS in mediating the cytotoxic effects of HG106. In our study, NAC at 10 mM marginally affected cell viability of A549 and H441 cells in vitro (Supplementary Figure 9), inconsistent with its tumor-promoting effect in mice (38), suggesting that the impact of antioxidants on tumor cell proliferation might depend on a long-term treatment process.

Oxidative stresses caused by ROS induce rapid depolarization of inner mitochondrial membrane potential (MMP) and subsequent impairment of oxidative phosphorylation, a function output of the tricarboxylic acid cycle (39). We next examined whether HG106 inhibited mitochondrial oxidative phosphorylation. As shown in Figure 6, C-D, HG106 dose-dependently reduced the oxygen consumption rate and disrupted

MMP in A549 and H441 cells. Using transmission electron microscopy, we also observed that cells treated with HG106 exhibited mitochondrial swelling, similar to the effects of hydrogen peroxide (Figure 6E). Accumulation of ROS concomitantly mediated endoplasmic reticulum (ER) stress (40). Our results further showed that HG106 increased the activation of the ER stress-related markers IRE1α, PERK and GRP78 (Figure 6F), and transcription of *CHOP*, *ATF4* and *ATF6* (Supplementary Figure 10). These data suggest that mitochondrial dysfunction and ER stress markedly occur in the presence of HG106 as a consequence of increased intracellular ROS levels.

Oncogenic RAS drives ROS production, and *KRAS*-mutant cells in turn show susceptibility to ROS-manipulation agents (33). We next examined the selective cytotoxicity of HG106 in *KRAS*-mutant cell lines. As expected, selective sensitivity between *KRAS*-mutant cell lines and their wild-type counterparts was observed in the presence of HG106 (Figure 6G). HG106 also displayed KRAS mutant selective killing towards the aforementioned panel of cancer cell lines (Figure 6H and Supplementary Table 9). Importantly, normal cells were less affected by HG106 when compared with *KRAS*-mutant ones (Supplementary Figure 11 and Supplementary Table 9), indicating the safety and low toxicity of HG106. Intriguingly, HG106 treatment did not lead to autophagy-related cell death (Supplementary Figure 12A) or ferroptosis (Supplementary Figure 12B). ROS-mediated mitochondrial dysfunction and elevated ER stress have been implicated in promoting tumor cell apoptosis (41). In accord with this, HG106 significantly induced apoptosis in *KRAS*-mutant LUAD cells (Figure 6I) and inhibited their colony formation (Figure 6J). All these results suggest that HG106 leads to a lethal increase in ROS levels in *KRAS*-mutant LUAD cells, causing selective cellular ER stress and apoptosis.

In vivo responses of *KRAS*-mutant LUAD to HG106.

On the basis of HG106 in vitro potency, we then explored its anti-tumor activity against *KRAS*-mutant LUAD in vivo in a series of preclinical mouse models. We first set up a lung cancer cell xenograft mouse model. A549 cells were injected s.c. into the flanks of 4–5-week-old male athymic nude mice. When tumors reached a volume about 150 mm^3, mice were treated with vehicle chow or different dosages of HG106 through daily intraperitoneal injection. As shown in Figure 7A, continuous HG106 treatment led to a prolonged tumor growth inhibition at tested doses. To investigate the HG106 efficacy at a more translational level, we then set up a patient-derived xenograft (PDX) model of LUAD harboring a G12V mutation in *KRAS*. After 3 weeks of treatment, HG106 strikingly suppressed PDX tumor growth as well (Figure 7B). Of note, the effect of HG106 therapy was well-tolerated since no animals in any group exhibited systematic toxicity in these studies (Supplementary Figure 13, A-B). Consistently, HG106 at doses of 2 or 4 mg/kg induced marked ROS production and TUNEL signal in patient-derived xenografts

(Supplementary Figure 14, A-B), validating that HG106 triggered ER stress-induced apoptosis in vivo.

In attempting to further explore the clinical benefit of HG106 in mouse survival, we carried out efficacy experiments in two conditional genetic models using the activation of oncogenic *KRAS* alone or in combination with the loss of function of *TRP53*. As shown in LSL-Kras^{G12D} mice, lung tumor volume (as assessed by micro CT imaging) was significantly reduced by HG106 (Supplementary Figure 15, A-B). The median survival in infected LSL-Kras^{G12D} vehicle mice was 39 days, whereas it was prolonged to 81 days or 106 days in two HG106-treated groups, respectively (Supplementary Figure 14C). Activation of an oncogenic allele of *KRAS* is sufficient to initiate the tumorigenesis process in lung, whereas additional deletion or point mutation of a tumor suppressor leads to a significantly faster development of adenocarcinomas that have features of more advanced disease, similar to that in humans (42). We thus set up the LSL-Kras$^{G12D/+}$;Trp53$^{flox/flox}$ conditional mouse model, and we found that the lung adenocarcinoma in the vehicle group grew aggressively and diffused quickly into the entire lung tissue over a 1-month period. However, HG106 treatment led to significant tumor inhibition compared to the vehicle group (P<0.001; Figure 7, C-D). More encouragingly, HG106 therapy produced a higher long-term survival advantage (log-rank test; P=0.0048; Figure 7E). Based on the convincing results from four preclinical mouse models, we confirmed that HG106 exhibited potent in vivo efficacy with a satisfactory therapeutic window for the treatment of lung adenocarcinoma.

Discussion

Approximately 30% of LUAD tumors carry mutations in *KRAS*, but no clinically applicable targeted strategy is yet available. To address this challenge, we profiled metabolic dysregulation in isogenic cell pairs with or without KRAS mutation to identify metabolic vulnerabilities for the treatment of *KRAS*-driven LUAD. We found dramatic changes in metabolites upon KRAS mutational activation, especially intermediates in glutathione biosynthesis. We further identified SLC7A11, a central regulator of adaptive glutathione metabolism by conferring specificity for cystine uptake, as a synthetic lethal target in *KRAS*-mutant LUAD (Figure 8A). In detail, we found that SLC7A11 was highly overexpressed in *KRAS*-mutant LUAD cells and tissues, displaying a significant association with tumor progression. Targeting SLC7A11 significantly impaired growth and survival of *KRAS*-mutant LUAD in vitro and in vivo, indicating that SLC7A11 was a functional and translatable target. More importantly, we successfully developed a potent SLC7A11 inhibitor, HG106, through a function-based chemical screen. SLC7A11 inhibition by HG106 selectively increased metabolic stress- and oxidative stress-mediated apoptosis in LUAD harboring *KRAS* mutations (Figure 8B). Overall, our findings demonstrate that suppression of the SLC7A11/glutathione axis causes metabolic lethality specifically in *KRAS*-mutant LUAD. The synthetic lethal link between KRAS mutational status and a requirement for SLC7A11 function may enable promising therapeutic approaches for the treatment of *KRAS*-mutant cancers.

Previous reports have indicated that *KRAS*-mutant tumor cells displayed distinct metabolic requirements compared to their wild-type counterparts (43). While these metabolic changes support growth and proliferation, they expose the Achilles' heel of cancer cells. Recently, a synthetic lethal screen carried out in a 3D clonogenic system identified inhibitors of dihydroorotate dehydrogenase that perturbed pyrimidine biosynthesis and selectively inhibited the growth of *KRAS*-mutant pancreatic cancer (44). SLC25A22, a mitochondrial glutamate transporter, has also been identified as a synthetic lethal partner of KRAS (45). All these studies support the notion that targeting metabolic synthetic lethality may be a promising approach for cancer therapy (16). In our study, we comprehensively revealed the glutathione dependence of *KRAS*-mutant cells. We found elevated endogenous glutathione levels coupled with increased cystine uptake in the presence of KRAS mutational activation (Figure 1). Glutathione plays a predominant anti-oxidative function in sustaining redox homeostasis. In response to redox equilibrium imbalance, *KRAS* mutant cells tend to enhance glutathione-mediated detoxification (30, 31). All our results agree with the notion that disrupting redox homeostasis, is an effective therapeutic option for *KRAS*-driven tumors (4, 32). Although it has become clear that tumors show varying degrees of reliance on oncogenic KRAS, due to metabolic variations, several aspects of how KRAS-dependence impacts metabolic rewiring (e.g., glutathione synthesis and redox homeostasis) and the

associated vulnerability in a complex tumor microenvironment remained to be determined.

Potential targeting metabolic alterations over-activated in a mutant KRAS context is critical. SLC7A11 has well-known functions serving as the specific antiporter of cystine intake (22, 46). SLC7A11 is upregulated in several types of cancer and represents an independent prognostic factor (20-24). In addition, SLC7A11 confers drug resistance by supplying cystine for glutathione maintenance (25-27) and represents an acquired vulnerability of MAPK inhibitor-resistant melanomas (26). Oncogenic KRAS and its effector pathways induce Nrf2, the master transcriptional regulator of endogenous antioxidant synthesis (34, 47). Knock down of *KRAS* or inhibition of PI3K suppressed Nrf2 activity and further regulated ATF4 (47). Inhibition of the MAPK pathway resulted in decreased induction of Nrf2 and its target genes via transcription factor Jun and Myc (34). In our study, we additionally incorporated Ral GTPase inhibitor RBC8 into experiments, and found that it could also lead to Nrf2 suppression, even though its efficacy was less than the MEK inhibitor, suggesting potential cooperativity of KRAS effector pathways in regulating Nrf2 transcription and function. In response to oxidative stress, Nrf2 in turn activates downstream elements including SLC7A11 (34, 48). However, the direct connection between SLC7A11 and mutant KRAS has not been clearly identified. Our results showed that mutant KRAS significantly promoted glutathione biosynthesis (Figure 1). In both KRAS isogenic cell lines and human *KRAS*-mutant LUAD tissues, SLC7A11 abundance was positively correlated with KRAS mutational activation, and this was in step with Nrf2 expression (Figure 2). Genetic disruption of *KRAS* decreased Nrf2, and key pathways downstream of KRAS shared the ability to modulate the Nrf2/SLC7A11 axis (Figure 2, E-H). Together with the published work demonstrating that *KRAS*-directed increase in Nrf2 expression is a mechanism for the activation of the Nrf2 antioxidant program (34), we proposed that Nrf2 might be a target of KRAS. Recently, Lim and colleagues independently revealed that cystine/glutamate transporter SLC7A11 is essential for *KRAS*-induced tumorigenicity by enhancing glutathione synthesis, and identified a synergy mechanism of transcription factors of ETS-1 and ATF4 in regulating SLC7A11 expression (49). ATF has been reported as both a transcriptional target and heterodimerization partner of Nrf2 (50, 51). Since there are *cis*-acting transcriptional regulatory elements present in the SLC7A11 promoter, it is likely several transcription factors (such as NRF2 and ATF4) could recognize them and share the ability and potential cooperativity to modulate SLC7A11 expression and function, particularly in cancer cells exhibiting an activated KRAS pathway. The dependence of *KRAS*-mutant cancers on increased glutathione biosynthesis could be therapeutically exploited through SLC7A11 silencing (Figure 3). Several agents have been characterized to suppress the transport activity of SLC7A11 (36), among which the most promising one is an FDA-approved agent, sulfasalazine, that is typically used to treat chronic inflammatory

disease (35). In accordance with the results of SLC7A11 genetic depletion, *KRAS*-mutant cells showed more sensitivity to sulfasalazine as well. Administration of sulfasalazine in the LSL-Kras^{G12D} mouse model significantly reduced tumor burden (Figure 4), consistent with previous studies about its in vivo anti-tumor activity in other types of cancer (19, 22, 25). Overall, these observations validate that *SLC7A11* is a synthetic lethal partner of *KRAS*, providing a direct link between these two factors.

Sulfasalazine inhibits SLC7A11 and leads to in vivo therapeutic effects; however, all current available SLC7A11 inhibitors, including sulfasalazine, have off-target effects, thereby limiting their use as SLC7A11-specific inhibitors in clinical settings (19). This was also evidenced by our results that sulfasalazine led to tumor regression at a substantially high dosage of 250 mg/kg in LSL-Kras^{G12D} mice (Figure 4). This prompted us to identify and develop highly potent SLC7A11 inhibitors. In this study, we showed that HG106 concentration-dependently blocked cystine uptake and glutathione biosynthesis by inhibiting SLC7A11 function. Metabolomic profiling further confirmed that glutathione metabolism was primarily inhibited by HG106, indicating its on-target effects (Figure 5). Specifically, suppression of SLC7A11 by HG106 markedly increased in the already-elevated levels of ROS and endoplasmic reticulum stress in *KRAS*-mutant cells, and consequently led to their apoptosis (Figure 6). Another genotype-selective compound erastin, identified by a chemical synthetic lethal screen, has been reported to be toxic to cells expressing RAS(G12V) (52). Further study revealed that the potency and activity of erastin was also associated with cystine depletion and impairment of SLC7A11-mediated cystine uptake (53, 54). In a way, the action and mechanism of our compound HG106 and erastin were quite similar since they both showed genotype-selective activity towards cells harboring RAS mutation through blocking SLC7A11. These data from small molecules further validates the synthetic lethal connection of *KRAS* and *SLC7A11*. However, differences in compound activity remain. HG106 exhibited selective lethality by inducing cell apoptosis, whereas erastin-treated cells undergo ferroptosis, a newly discovered cell death mechanism (53). This may be explained by the differential chemical structures of the two drugs and diversity in elevated ROS-mediated cell death (55).

Considering the potency of the current available SLC7A11 inhibitors, the potential approach to achieve clinical benefit from SLC7A11 inhibition would be to conduct combination therapies. Several lines of evidence demonstrated a synergistic benefit of combined inhibition of SLC7A11 and other targets. SLC7A11 suppression by HDAC inhibitors could result in active cell death in BRAF inhibitor-resistant cells (26). In addition, it has been reported that suppression of SLC7A11 showed a strong synergy with mutant-p53 reactivators by glutathione depletion and massive apoptosis in *TP53*-mutant cancer cells (41). In light of all this evidence, it might be promising to combine HG106 with other clinical agents, such as MEK inhibitors or chemotherapeutics, to

fundamentally defeat *KRAS*-mutant LUAD. In summary, we identify a druggable synthetic lethal interaction between *SLC7A11* and *KRAS*, enlightening promising therapeutic perspectives for *KRAS*-mutant lung adenocarcinoma.

Methods

Detailed protocols are provided in the Supplementary Methods.

Cell lines and culture

The immortalized and non-tumorigenic pancreatic epithelial HPNE cells and their transformed counterparts HPNE/KRAS were generated and reported previously (28). Briefly, mutant KRAS(G12V) was introduced into HPNE cells through lentivirus delivery system. The H522/KRAS cells were generated by introduction of a KRAS (G12C) mutation into H522 cells through an adeno-associated virus (AAV) system (Addgene, Cambridge, MA). In brief, AAV-KRAS(G12C) or corresponding empty vector, together with AAV helper plasmid (Rep/Cap) and pHGTI-adeno1, were transfected into 293T cells, respectively. Adeno-associated virus was generated, collected and sequentially used to infect H522 cells in the presence of 10 μg/mL of polybrene (Millipore, Billerica, MA). After 48 h of infection, monoclonal populations harboring KRAS(G12C) were purified and selected by puromycin (Sangon Biotech, Shanghai, China). Active KRAS (KRAS-GTP) in monoclonal cells was pulled down with Raf-1 RBD agarose beads (Millipore, Billerica, MA) and examined by Western blotting assays. The positive monoclones were further identified using Sanger sequencing (BioSune, Shanghai, China). Detailed cell origins and growth conditions are provided in the Supplementary Methods. All of the cell lines were authenticated by short tandem repeat analysis before use.

Metabolomic profiling

HPNE and HPNE/KRAS cells were directly harvested without any treatments. A549 cells were plated and treated with HG106 (5 μM) for 6 h. Cells were collected by scraping and cell pellets from these two sets of samples were immediately flash-frozen in liquid nitrogen and stored at -80 °C until extraction. The changes in metabolites were examined by gas chromatography with time-of-flight mass spectrometry-based metabolomics as previously described (56). See Supplementary Methods for details regarding metabolite profiling and pathway analysis.

[^{14}C]-cystine uptake

Cells were plated at a density of 100,000 cells per well in 12-well plates. After overnight adherence, cells were treated with sulfasalazine (1 mM, 3 min) or HG106 (1.25, 2.5, 5, 10 μM, 3 min), respectively. Cells were then washed with phosphate-buffered saline and incubated in pre-warmed Na^+-free buffer at 37 °C for 10 min. After that, L-[3,3'-^{14}C]-cystine (0.2 μCi/mL; Perkin Elmer, Waltham, MA) was added for 15 min.

Cells were lysed with 200 μL of 0.1 M NaOH solution, and scintillation fluid was sequentially added into harvested cell lysates. Radioactive [^{14}C] counts per minute were obtained using Beckman Coulter LS 6500 Liquid Scintillation Counter.

Glutathione detection

Cells were plated in 6-well plates at a density of 800,000 to 1000,000 cells per well. Cells were treated with sulfasalazine (1 mM, 12 h) or HG106 (1.25, 2.5, 5, 10 μM, 12 h). Glutathione levels were evaluated using a GSH/GSSG-Glo^{TM} assay kit (Promega, Madison, WI) following the manufacturer's instructions. Glutathione concentration was calculated from an internal standard curve and normalized to total cell number as determined from parallel plates.

Evaluation of reactive oxygen species

Isogenic cell pairs were harvested at 48 h after si*SLC7A11* transfection. A549 cells were treated with H_2O_2 (16 mM, 1 h) or HG106 (2.5, 5, 10 μM, 6 h) in 6-well plates at a density of 300,000 to 500,000 cells per well. All the cells were harvested in conditional Dulbecco's modified Eagle's medium containing DCFH-DA (25 μM; Sigma, St. Louis, MO). After incubation at 37 °C for 30 min, cells were washed with phosphate-buffered saline and subjected to flow cytometry (FACSCanto II system, BD).

A549 xenograft, patient-derived LUAD xenograft and autochthonous murine lung cancer models

C57BL/6 and BALB/cA nude mice were purchased from National Rodent Laboratory Animal Resources (Shanghai, China). LSL-Kras$^{G12D/+}$;Trp53$^{flox/flox}$ (KP; B6.129-Kras^{tm4Tyj} Trp53$^{tm1Brn/J}$) mice on a C57BL/6J background were purchased from the Jackson Laboratory (Sacramento, CA). Animals were caged in a laminar airflow cabinet under specific pathogen-free conditions, fed with sterilized food and water, and kept on a 12-h light/dark cycle. Briefly, 6-week-old BALB/cA nude mice were used to generate A549 xenograft and patient-derived LUAD xenograft mouse models. For the A549 xenograft mouse model, A549 cells (5×10^6) were injected subcutaneously into mice. For the human primary LAUD xenograft, fragments from a poorly differentiated LAUD harboring a KRAS(G12V) mutation that were obtained from treatment-naive patients at the Shanghai Changzheng Hospital (Shanghai, China) were implanted subcutaneously into mice (57). After inoculation of cells or tissues, mice were monitored until tumor volumes grew to 100-200 mm^3. Tumor volume was calculated using the following formula: (length × width × width × 0.52). After that, the mice were randomized into four groups and treated with vehicle or different dosages of HG106 for about one month. HG106 was dissolved in 0.5 % sodium carboxymethylcellulose (CMC-Na) and delivered daily by intraperitoneal injections. Mice intraperitoneally injected with 0.5% CMC-Na served as

the vehicle control. Tumor volumes were measured every other day and the mouse body weight was recorded in parallel. After the last day of treatment, tumors were excised and weighed as an indicator of tumor burden.

LSL-Kras$^{G12D/+;}$Trp53$^{flox/flox}$ mice were used as an autochthonous model for *KRAS*-mutant adenocarcinomas in this study. In the KP mouse model, intra-tracheal delivery of adenovirus expressing Cre induced oncogenic Kras activation in lung airway cells and led to the formation of aggressive adenocarcinomas. In brief, 8-week-old KP mice were anesthetized with isoflurane via a gas chamber. Adeno-Cre (HanBio, Shanghai, China) at a dose of 2.5× 10^7 PFU in a total volume of 125 μL was introduced into mice. Five weeks after virus inhalation, lungs were imaged by Quantum GX microCT Imaging System (PerkinElmer Inc., Hopkington, MA) in order to confirm tumor formation. After tumor formation, animals were randomized into two groups treated with HG106 at dosage of 4 mg/kg/d. HG106 was dissolved in 0.5% CMC-Na and delivered daily by intraperitoneal injections. In parallel, mice intraperitoneally injected with 0.5% CMC-Na served as the vehicle control. Multi-focal adenocarcinomas in mice were measured during the treatment. The survival curves were calculated by the Kaplan-Meier method. Statistical significance was assessed by the log-rank test.

Statistics

Unless otherwise noted, data were expressed as mean ± SD. One-way ANOVA or 2-tail student's *t*-test was used to compare the means among groups. The log-rank test was used to compare Kaplan-Meier survival curves. Statistical tests were performed by Microsoft Excel or GraphPad Prism Software version 5.0. Significance was set at $P<0.05$.

Study approval

All animal treatments were performed according to the guidelines of Institution Animal Care and Use Committee (NIH) and all the protocols were approved by East China Normal University. Human LUAD tissue was obtained from the General Hospital of Ningxia Medical University (Ningxia, China) in accordance with approval from the ethics committee. Prior written informed consent was obtained from patients.

Authors' contributions

KH, YC, ML, and XP designed and supervised the research. KH, KL, JL, JC, HW, WJ, JW, HP, and ZC performed research and provide helpful discussions. KH, KL, JL, JF, JC, HW, FC, WJ, JW, HP, ZC, YC, ML and XP analyzed and interpreted the data. JF and FC developed the data clustering and performed bioinformatics analysis. JC collected patient samples and conducted pathology evaluations. HW, HP and YC conducted chemical synthesis. PJC generated and provided KRAS isogenic cell lines. KH, KL, JL,

XP, and other authors wrote the manuscript. All authors reviewed and edited the manuscript. KH, KL and JL equally contributed as first authors. KH was chosen as the first because he led the project and played a fundamental role in all phases of the study. KL set up all the animal models and evaluated in vivo efficacy of drugs. JL had a primary role in interpreting and organizing the data as well as writing the manuscript.

Acknowledgments

We thank Dr. Hongbin Ji (Shanghai Institute of Biochemistry and Cell Biology, Chinese Academy of Sciences, Shanghai, China) for helping us to set up KP mouse models. We thank Dr. Stefan Siwko (Texas A&M University Health Science Center, Institute of Biosciences and Technology, Houston, Texas) for manuscript editing. This work is sponsored by Shanghai Pujiang Program (18PJD014 to XP), National Natural Science Foundation of China (81672758 and 81874207 to XP; 81830083 to ML; 81673304 to YC), Innovation Program of Shanghai Municipal Education Commission (2017-01-07-00-05-E00011 to ML), and the Fundamental Research Funds for the Central Universities (40500-20101-222141 to XP).

References

1. Simanshu DK, Nissley DV, and McCormick F. RAS Proteins and Their Regulators in Human Disease. *Cell.* 2017;170(1):17-33.
2. Rotow J, and Bivona TG. Understanding and targeting resistance mechanisms in NSCLC. *Nat Rev Cancer.* 2017;17(11):637-658.
3. Kris MG, et al. Using multiplexed assays of oncogenic drivers in lung cancers to select targeted drugs. *JAMA.* 2014;311(19):1998-2006.
4. Cox AD, Fesik SW, Kimmelman AC, Luo J, and Der CJ. Drugging the undruggable RAS: Mission possible? *Nat Rev Drug Discov.* 2014;13(11):828-851.
5. Cancer Genome Atlas Research N. Comprehensive molecular profiling of lung adenocarcinoma. *Nature.* 2014;511(7511):543-550.
6. Janes MR, et al. Targeting KRAS Mutant Cancers with a Covalent G12C-Specific Inhibitor. *Cell.* 2018;172(3):578-589.
7. AMG 510 First to Inhibit "Undruggable" KRAS. *Cancer Discov.* 2019;9(8):988-989.
8. Hallin J, et al. The KRASG12C Inhibitor, MRTX849, Provides Insight Toward Therapeutic Susceptibility of KRAS Mutant Cancers in Mouse Models and Patients. *Cancer Discov.* 2019.
9. Canon J, et al. The clinical KRAS(G12C) inhibitor AMG 510 drives anti-tumour immunity. *Nature.* 2019;575(7781):217-223.
10. Samatar AA, and Poulikakos PI. Targeting RAS-ERK signalling in cancer: promises and challenges. *Nat Rev Drug Discov.* 2014;13(12):928-942.
11. Janne PA, et al. Selumetinib Plus Docetaxel Compared With Docetaxel Alone and Progression-Free Survival in Patients With KRAS-Mutant Advanced Non-Small Cell Lung Cancer: The SELECT-1 Randomized Clinical Trial. *JAMA.* 2017;317(18):1844-1853.
12. Turke AB, et al. MEK inhibition leads to PI3K/AKT activation by relieving a negative feedback on ERBB receptors. *Cancer Res.* 2012;72(13):3228-3237.
13. Ambrogio C, et al. KRAS Dimerization Impacts MEK Inhibitor Sensitivity and Oncogenic Activity of Mutant KRAS. *Cell.* 2018;172(4):857-868.
14. Lv J, Wang J, Chang S, Liu M, and Pang X. The greedy nature of mutant RAS: a boon for drug discovery targeting cancer metabolism? *Acta Biochim Biophys Sin (Shanghai).* 2016;48(1):17-26.
15. Kerr EM, and Martins CP. Metabolic rewiring in mutant Kras lung cancer. *FEBS J.* 2018;285(1):28-41.
16. Zecchini V, and Frezza C. Metabolic synthetic lethality in cancer therapy. *Biochim Biophys Acta.* 2017;1858(8):723-731.
17. Ying H, et al. Oncogenic Kras maintains pancreatic tumors through regulation of anabolic glucose metabolism. *Cell.* 2012;149(3):656-670.
18. Son J, et al. Glutamine supports pancreatic cancer growth through a KRAS-regulated

metabolic pathway. *Nature.* 2013;496(7443):101-105.

19. Koppula P, Zhang Y, Zhuang L, and Gan B. Amino acid transporter SLC7A11/xCT at the crossroads of regulating redox homeostasis and nutrient dependency of cancer. *Cancer Commun (Lond).* 2018;38(1):12.
20. Savaskan NE, et al. Small interfering RNA-mediated xCT silencing in gliomas inhibits neurodegeneration and alleviates brain edema. *Nat Med.* 2008;14(6):629-632.
21. Zhang L, et al. Overexpression of SLC7A11: a novel oncogene and an indicator of unfavorable prognosis for liver carcinoma. *Future Oncol.* 2018;14(10):927-936.
22. Timmerman LA, et al. Glutamine sensitivity analysis identifies the xCT antiporter as a common triple-negative breast tumor therapeutic target. *Cancer Cell.* 2013;24(4):450-465.
23. Ji X, et al. xCT (SLC7A11)-mediated metabolic reprogramming promotes non-small cell lung cancer progression. *Oncogene.* 2018;37(36):5007-5019.
24. Robert SM, et al. SLC7A11 expression is associated with seizures and predicts poor survival in patients with malignant glioma. *Sci Transl Med.* 2015;7(289):289ra86.
25. Huang Y, Dai Z, Barbacioru C, and Sadee W. Cystine-glutamate transporter SLC7A11 in cancer chemosensitivity and chemoresistance. *Cancer Res.* 2005;65(16):7446-7454.
26. Wang L, et al. An Acquired Vulnerability of Drug-Resistant Melanoma with Therapeutic Potential. *Cell.* 2018;173(6):1413-1425.
27. Lo M, Ling V, Wang YZ, and Gout PW. The xc- cystine/glutamate antiporter: a mediator of pancreatic cancer growth with a role in drug resistance. *Br J Cancer.* 2008;99(3):464-472.
28. Chang Z, et al. Cooperativity of oncogenic K-ras and downregulated p16/INK4A in human pancreatic tumorigenesis. *PLoS One.* 2014;9(7):e101452.
29. Miyanishi K, et al. Glutathione S-transferase-pi overexpression is closely associated with K-ras mutation during human colon carcinogenesis. *Gastroenterology.* 2001;121(4):865-874.
30. De Raedt T, et al. Exploiting cancer cell vulnerabilities to develop a combination therapy for ras-driven tumors. *Cancer Cell.* 2011;20(3):400-413.
31. Kerr EM, Gaude E, Turrell FK, Frezza C, and Martins CP. Mutant Kras copy number defines metabolic reprogramming and therapeutic susceptibilities. *Nature.* 2016;531(7592):110-113.
32. Kawamura T, Kondoh Y, Muroi M, Kawatani M, and Osada H. A small molecule that induces reactive oxygen species via cellular glutathione depletion. *Biochem J.* 2014;463(1):53-63.
33. Weinberg F, et al. Mitochondrial metabolism and ROS generation are essential for Kras-mediated tumorigenicity. *Proc Natl Acad Sci U S A.* 2010;107(19):8788-8793.
34. DeNicola GM, et al. Oncogene-induced Nrf2 transcription promotes ROS

detoxification and tumorigenesis. *Nature.* 2011;475(7354):106-109.

35. Gout PW, Buckley AR, Simms CR, and Bruchovsky N. Sulfasalazine, a potent suppressor of lymphoma growth by inhibition of the x(c)- cystine transporter: a new action for an old drug. *Leukemia.* 2001;15(10):1633-1640.
36. Dixon SJ, et al. Ferroptosis: an iron-dependent form of nonapoptotic cell death. *Cell.* 2012;149(5):1060-1072.
37. Ishii T, Bannai S, and Sugita Y. Mechanism of growth stimulation of L1210 cells by 2-mercaptoethanol in vitro. Role of the mixed disulfide of 2-mercaptoethanol and cysteine. *J Biol Chem.* 1981;256(23):12387-12392.
38. Sayin VI, et al. Antioxidants accelerate lung cancer progression in mice. *Sci Transl Med.* 2014;6(221):221ra15.
39. Hu Y, et al. K-ras(G12V) transformation leads to mitochondrial dysfunction and a metabolic switch from oxidative phosphorylation to glycolysis. *Cell Res.* 2012;22(2):399-412.
40. Verfaillie T, et al. PERK is required at the ER-mitochondrial contact sites to convey apoptosis after ROS-based ER stress. *Cell Death Differ.* 2012;19(11):1880-1891.
41. Liu DS, et al. Inhibiting the system xC(-)/glutathione axis selectively targets cancers with mutant-p53 accumulation. *Nat Commun.* 2017;8:14844.
42. DuPage M, Dooley AL, and Jacks T. Conditional mouse lung cancer models using adenoviral or lentiviral delivery of Cre recombinase. *Nat Protoc.* 2009;4(7):1064-1072.
43. Kimmelman AC. Metabolic Dependencies in RAS-Driven Cancers. *Clin Cancer Res.* 2015;21(8):1828-1834.
44. Koundinya M, et al. Dependence on the Pyrimidine Biosynthetic Enzyme DHODH Is a Synthetic Lethal Vulnerability in Mutant KRAS-Driven Cancers. *Cell Chem Biol.* 2018;25(6):705-717.
45. Wong CC, et al. SLC25A22 Promotes Proliferation and Survival of Colorectal Cancer Cells With KRAS Mutations and Xenograft Tumor Progression in Mice via Intracellular Synthesis of Aspartate. *Gastroenterology.* 2016;151(5):945-960.
46. Sato H, Tamba M, Ishii T, and Bannai S. Cloning and expression of a plasma membrane cystine/glutamate exchange transporter composed of two distinct proteins. *J Biol Chem.* 1999;274(17):11455-11458.
47. Gwinn DM, et al. Oncogenic KRAS Regulates Amino Acid Homeostasis and Asparagine Biosynthesis via ATF4 and Alters Sensitivity to L-Asparaginase. *Cancer Cell.* 2018;33(1):91-107.
48. Chen D, et al. NRF2 Is a Major Target of ARF in p53-Independent Tumor Suppression. *Mol Cell.* 2017;68(1):224-232.
49. Lim JKM, et al. Cystine/glutamate antiporter xCT (SLC7A11) facilitates oncogenic RAS transformation by preserving intracellular redox balance. *Proc Natl Acad Sci U S A.* 2019;116(19):9433-9442.

50. He CH, et al. Identification of activating transcription factor 4 (ATF4) as an Nrf2-interacting protein. Implication for heme oxygenase-1 gene regulation. *J Biol Chem.* 2001;276(24):20858-20865.
51. Ye P, et al. Nrf2- and ATF4-dependent upregulation of xCT modulates the sensitivity of T24 bladder carcinoma cells to proteasome inhibition. *Mol Cell Biol.* 2014;34(18):3421-3434.
52. Dolma S, Lessnick SL, Hahn WC, and Stockwell BR. Identification of genotype-selective antitumor agents using synthetic lethal chemical screening in engineered human tumor cells. *Cancer Cell.* 2003;3(3):285-296.
53. Stockwell BR, et al. Ferroptosis: A Regulated Cell Death Nexus Linking Metabolism, Redox Biology, and Disease. *Cell.* 2017;171(2):273-285.
54. Dixon SJ, et al. Pharmacological inhibition of cystine-glutamate exchange induces endoplasmic reticulum stress and ferroptosis. *Elife.* 2014;3:e02523.
55. Galluzzi L, et al. Molecular mechanisms of cell death: recommendations of the Nomenclature Committee on Cell Death 2018. *Cell Death Differ.* 2018;25(3):486-541.
56. Kind T, et al. FiehnLib: mass spectral and retention index libraries for metabolomics based on quadrupole and time-of-flight gas chromatography/mass spectrometry. *Anal Chem.* 2009;81(24):10038-10048.
57. Wang J, et al. Suppression of KRas-mutant cancer through the combined inhibition of KRAS with PLK1 and ROCK. *Nat Commun.* 2016;7:11363.

Figures and figure legends

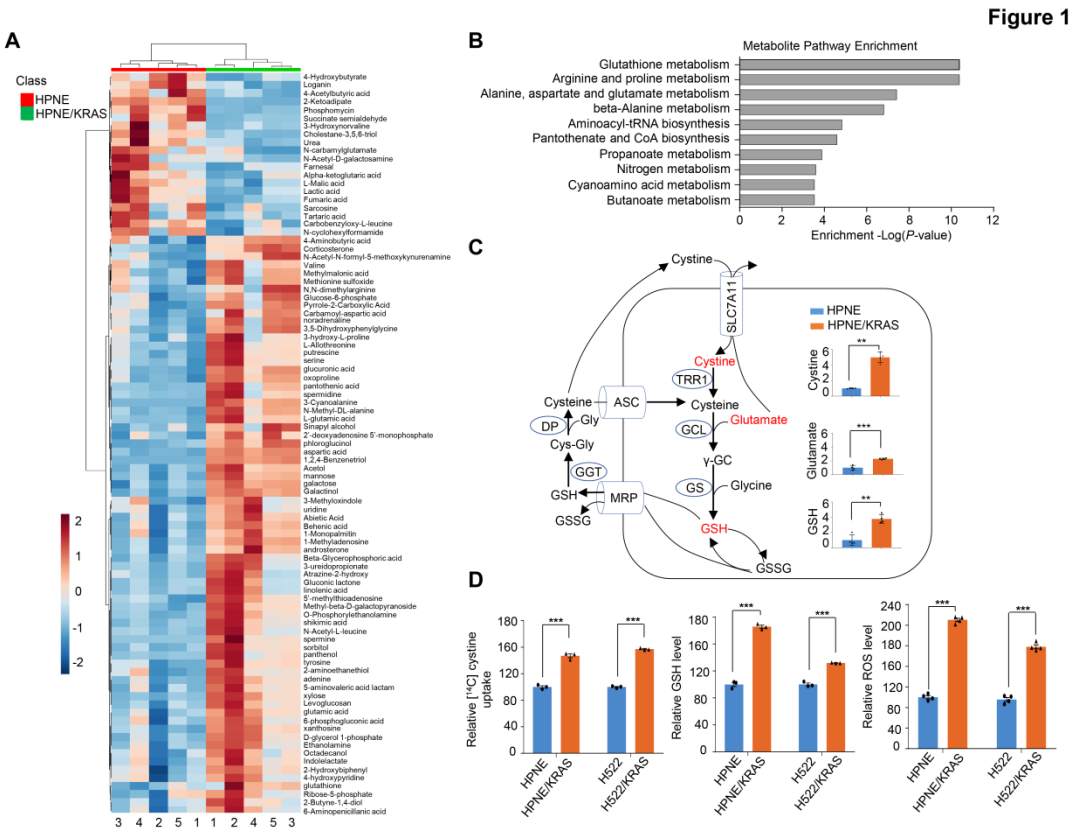

Figure 1. Mutant KRAS drives glutathione (GSH) metabolism reprogramming. (**A**) Heatmap showing significantly different metabolites (P<0.05) between HPNE and HPNE/KRAS groups. Values are scaled as indicated (2 to −2), (n=5). (**B**) The top 10 enriched pathways from integrated pathway analysis of significantly changed metabolites. The P-value cut-off is 0.05 and denoted the significance of the pathway. (**C**) Illustration of the GSH metabolism pathway (*left*) and the relative levels of cystine, glutamate and GSH (*right*), (n=5). (**D**) Cystine (*left*), GSH (*middle*) and reactive oxygen species (ROS) levels (*right*) quantified in KRAS isogenic cell lines. Na^+-independent [^{14}C]-cystine uptake was analyzed by a scintillation counter. The intracellular GSH content was measured using a GSH/GSSG-Glo^{TM} assay kit. For the determination of ROS production, the cells were loaded with DCFH-DA and the fluorescence intensity was measured by flow cytometry. The levels in KRAS wild-type cells are defined as 100%. Results shown are representative of 3 independent experiments. Data are represented as mean ± SD of biological triplicates. **P<0.01; ***P<0.001 by unpaired, 2-tailed Student's t-tests.

Figure 2

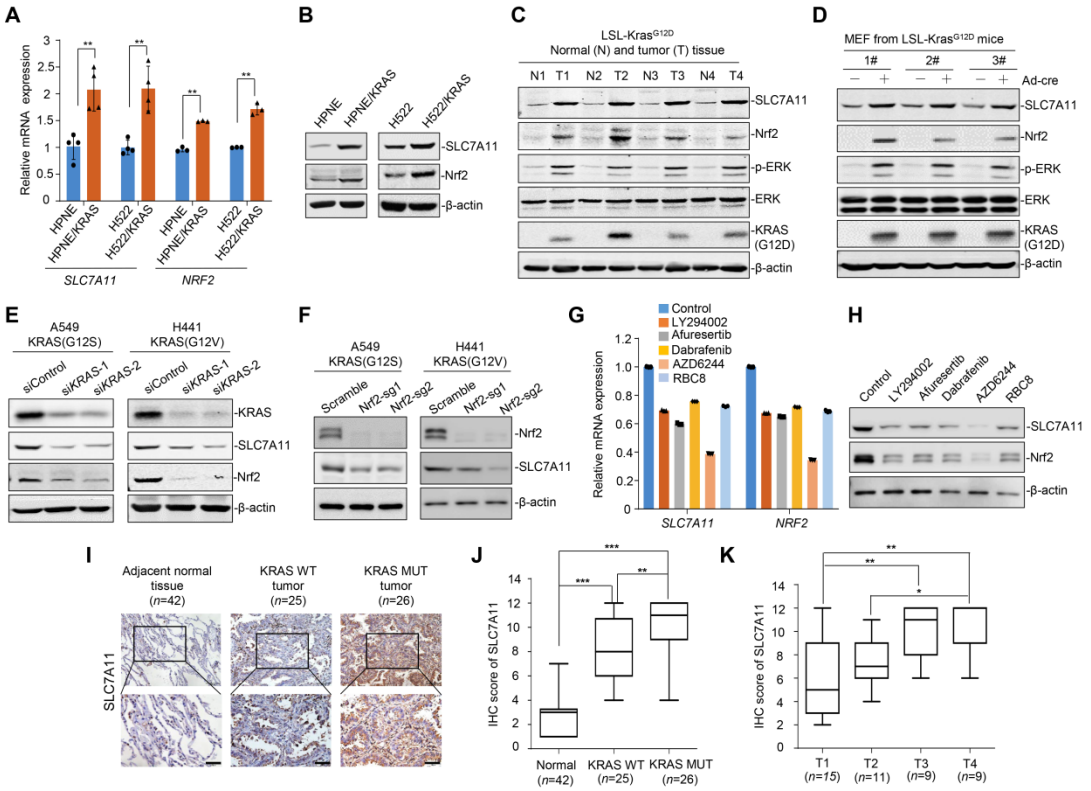

Figure 2. SLC7A11 is overexpressed in *KRAS*-mutant LUAD. (**A**) The mRNA levels of *SLC7A11* and *NRF2*. (**B**) The protein levels of SLC7A11 and Nrf2. For each cell pair, SLC7A11 and Nrf2 are contemporaneous immunoblots that run in parallel from the same biological replicate. (**C**) SLC7A11 and Nrf2 expression in normal lung tissues (N) and tumors (T) from LSL-Kras^{G12D} mice (n= 4). p-ERK was stripped and the same membrane was then immunoblotted for total ERK. (**D**) Nrf2 and SLC7A11 expression in mouse embryonic fibroblasts (MEF) cells. MEF cells were generated from LSL-Kras^{G12D} mice and induced by adenovirus-Cre for 48 h (n=3). p-ERK and total ERK are contemporaneous immunoblots that run in parallel from the same biological replicate. (**E**) Nrf2 and SLC7A11 expression upon KRAS silencing. For individual cell line, KRAS, SLC7A11 and Nrf2 are contemporaneous immunoblots that run in parallel from the same biological replicate. (**F**) SLC7A11 suppression upon genetic depletion of Nrf2. (**G**) and (**H**) SLC7A11 and Nrf2 expression upon blockade of KRAS signaling at mRNA (**G**) and protein levels (**H**). A549 cells were treated with LY2940022 (1 μM, PI3K inhibitor), afuresertib (5 μM, Akt inhibitor), dabrafenib (20 μM, Raf inhibitor), AZD6244 (20 nM, MEK inhibitor) and RBC8 (10 μM, Ral GTPase inhibitor) for 48 h, respectively. Results are shown as mean ± SD of biological triplicates. **P<0.01 by unpaired, 2-tailed Student's t-tests. (**I**) SLC7A11 expression in clinical samples. Scale bars, 50 μm. (**J**) Box plots showing SLC7A11 immunohistochemistry scores. The horizontal lines representing the median; the bottom and top of the boxes represent the 25th and 75th percentiles, respectively; and the vertical bars representing the range of the data. (**K**) Box plot of SLC7A11 expression in clinical

tumors. Stage classification of LUAD refers to the TNM classification. *P<0.05; **P<0.01; ***P<0.001 by one-way ANOVA with Tukey's multiple comparison test.

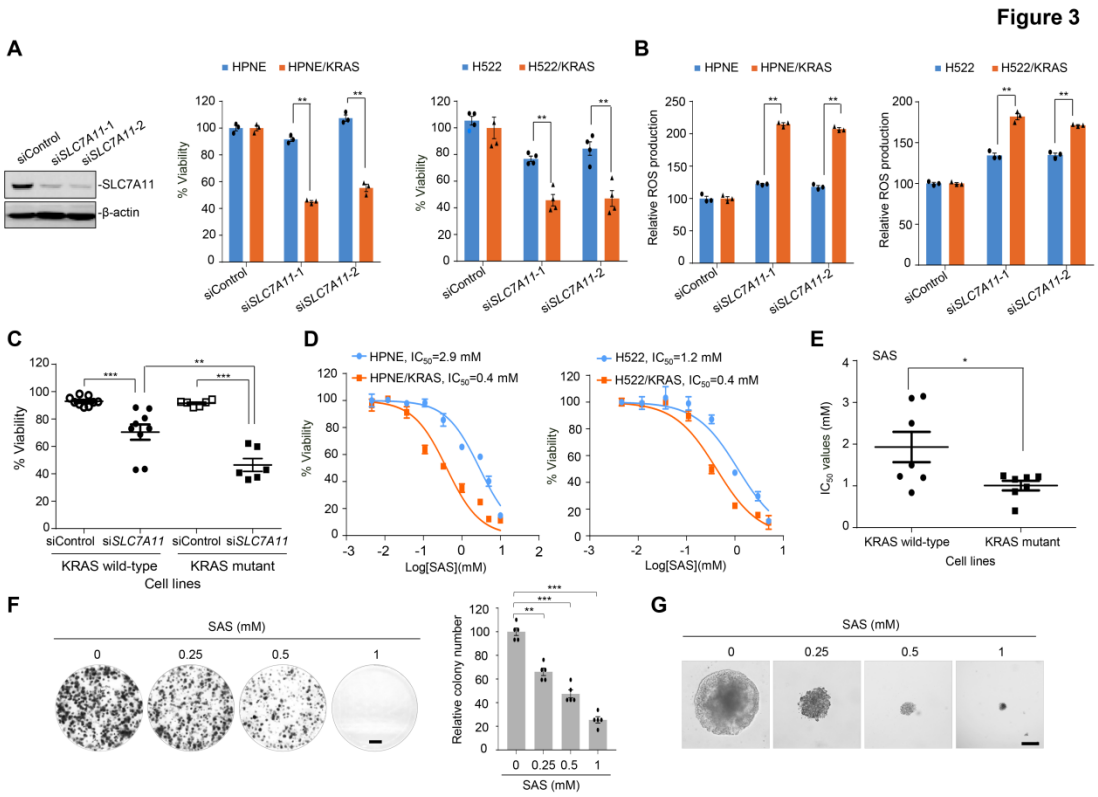

Figure 3. Silencing SLC7A11 selectively kills *KRAS*-mutant LUAD cells. (**A**) The effects of SLC7A11 depletion on cell survival. Isogenic cells were transfected with SLC7A11 siRNAs (si*SLC7A11*) or a scrambled siRNA (siControl). The knockdown efficiency of si*SLC7A11* was examined by immunoblotting (*left*). Cell viability was measured 72 h posttransfection (*right*). The relative cell viability was calculated by setting the values of siControl alone group as 100%. (**B**) The effects of SLC7A11 depletion on ROS production. The relative ROS production was calculated by setting the values of siControl alone group as 100%. (**C**) SLC7A11 depletion led to selective toxicity towards *KRAS*-mutant cancer cell lines. Six *KRAS*-mutant and nine wild-type cancer cell lines (see Supplementary Table 3) were transfected with si*SLC7A11* or a scrambled siRNA, respectively. The percent cell viability is relative to the untreated controls. (**D**) The inhibitory effects of sulfasalazine (SAS) on isogenic cell lines. (**E**) SAS treatment led to selective toxicity towards *KRAS*-mutant cancer cells. Seven *KRAS*-mutant and seven wild-type cancer cell lines were treated with SAS for 72 h. *Dots*, IC_{50}s of each cell lines. (**F**) Colony formation of A549 cells after SAS treatment. A549 cells were plated in the 6-well plates and treated with indicated concentrations of SAS for 7 days. The relative number of colonies is calculated by normalization to untreated group as 100%. Scale bars, 0.5 cm. (**G**) Effect of SAS on A549 cell soft-agar colony formation. A549 cells were uniformly dispersed in agar and treated with indicated concentrations of SAS for 21 days. The medium containing SAS was changed twice a week. At the end of the experiment, the colonies were photographed. Scale bars, 2 mm. All data are representative of 3

independent experiments, and shown as mean ± SD of biological triplicates. *P<0.05, **P<0.01, ***P<0.001 by unpaired, 2-tailed Student's t-tests.

Figure 4

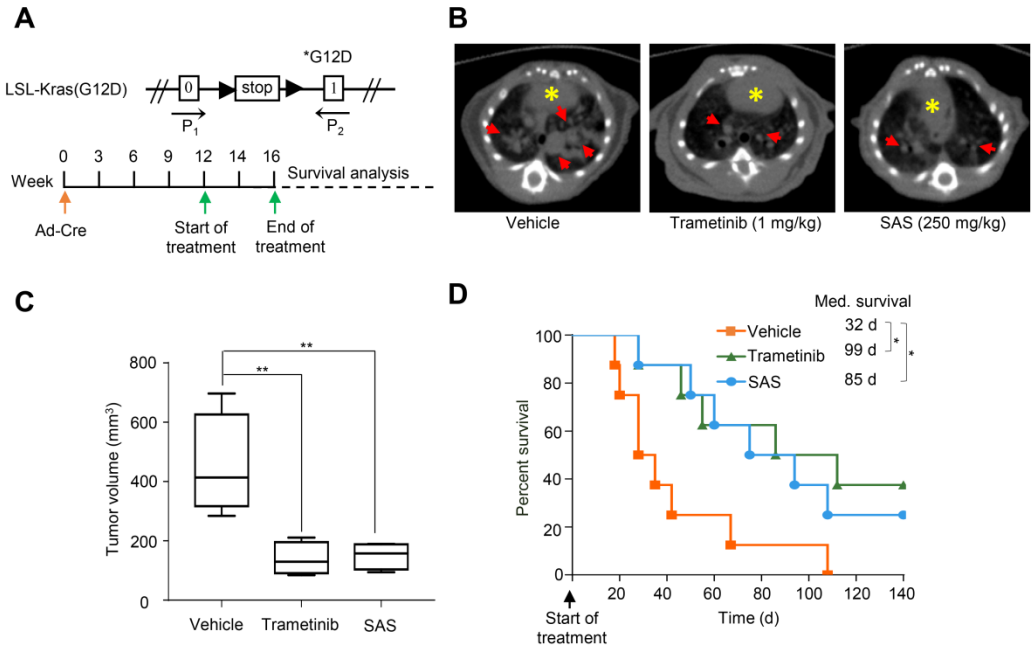

Figure 4. Sulfasalazine leads to tumor regression in vivo. (**A**) Schematic illustration of the LSL-Kras^{G12D} allele and drug treatment protocol. LSL-Kras^{G12D} mice were induced with adenovirus-Cre. After 12-week induction, mice were treated with vehicle, trametinib (1 mg/kg) or sulfasalazine (SAS, 250 mg/kg) for additional 4 weeks. (**B**) Representative tumor images of LSL-Kras^{G12D} mice. Animals were scanned by micro-computed tomography. Red arrows indicate lung tumors, and yellow stars indicate heart. (**C**) Box plots showing the tumor volumes at the endpoint of indicated treatments based on micro-CT (n=5). The horizontal lines representing the median; the bottom and top of the boxes representing the 25th and 75th percentiles, respectively; and the vertical bars representing the range of the data. All data are shown as mean ± SD. **P<0.01 by one-way ANOVA with Tukey's multiple comparison test. (**D**) Kaplan-Meier survival curves of LSL-Kras^{G12D} mice after indicated treatments (n=8). *P<0.05 by log-rank tests.

Figure 5

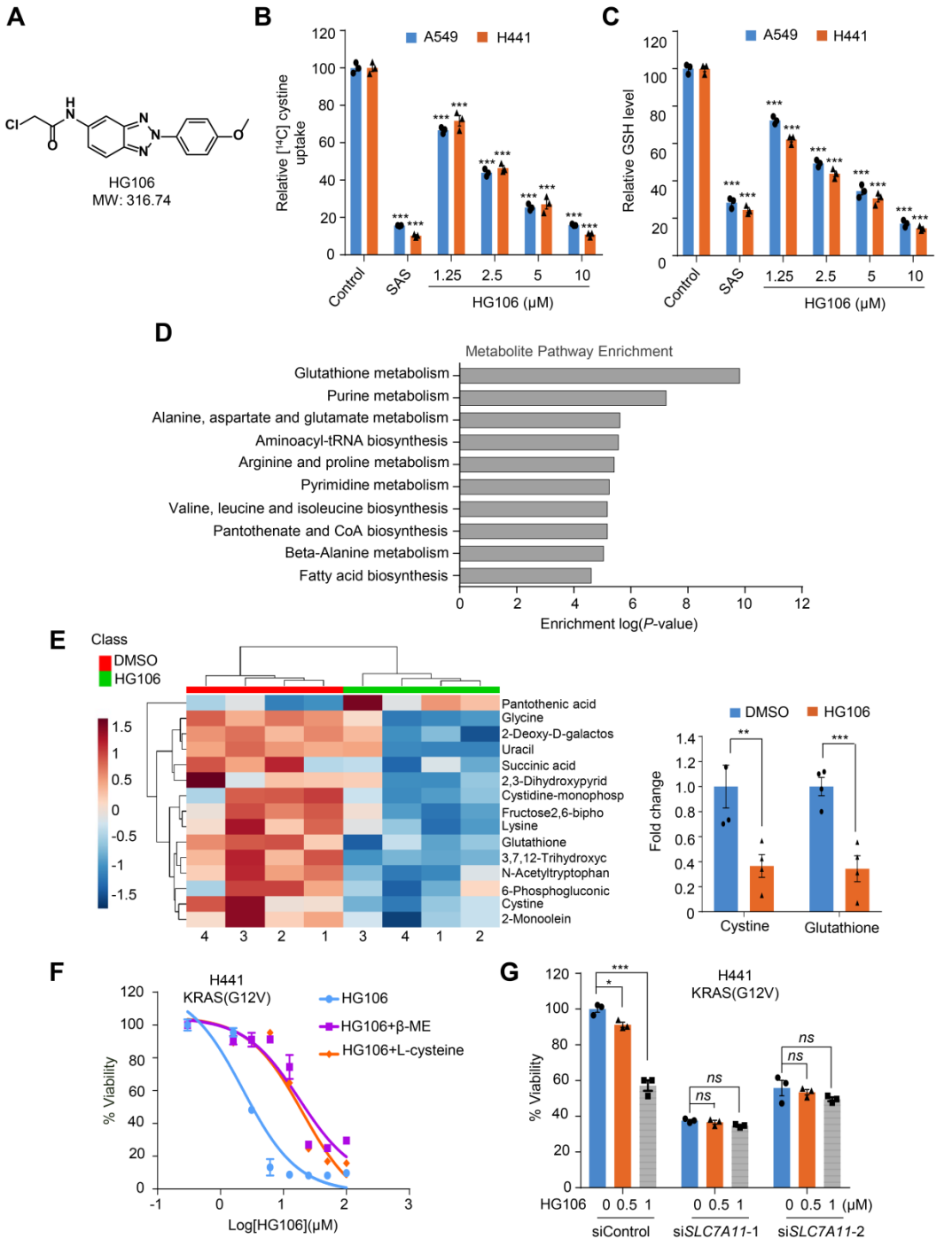

Figure 5. Identification of HG106 as a potent SLC7A11 inhibitor. (**A**) Chemical structure of HG106. (**B**) and (**C**) HG106 dose-dependently inhibited cystine uptake and glutathione (GSH) level. A549 and H441 cells were treated with HG106 and sulfasalazine (SAS, 1 mM). The relative cystine uptake and GSH levels are calculated by setting the values of the vehicle control group as 100%. (**D**) Metabolic pathway enrichment in A549 cells after HG106 treatment. A549 cells were treated with 5 μM HG106 for 6 h. Cell lysates were subjected to metabolomic profiling. For metabolite pathway enrichment

analysis, subsets of significantly affected metabolites are chosen. The bar plot shows the top 10 enriched pathways (*n*=4). (**E**) The significantly changed metabolites involved in GSH biosynthesis are shown in the heatmap (*left*), (*n*=4). The changes of cystine and glutathione between the vehicle control and HG106-treated groups are shown according to the metabolomic data (*right*). (**F**) Effect of β-mercaptoethanol (β-ME, 100 μM) and L-cysteine (5 mM) on HG106-induced cell death in H441 cells. H441 cells were treated with HG106 concentration gradient with or without β-ME and L-cysteine for 72 h, and cell viability was measured. (**G**) Effect of SLC7A11 knockdown by RNA interference on HG106-induced cell death. H441 cells were treated with indicated concentration of HG106 72 h posttransfection with SLC7A11 siRNAs or a scrambled siRNA. The relative cell viability is calculated by setting the values of siControl group as 100%. All data are representative of at least 2 independent experiments, and shown as mean ± SD of biological triplicates. **P*<0.05, ***P*<0.01, ****P*<0.001 by one-way ANOVA with Tukey's multiple comparison test (B, C, and G), or by unpaired, 2-tailed Student's *t*-tests (E).

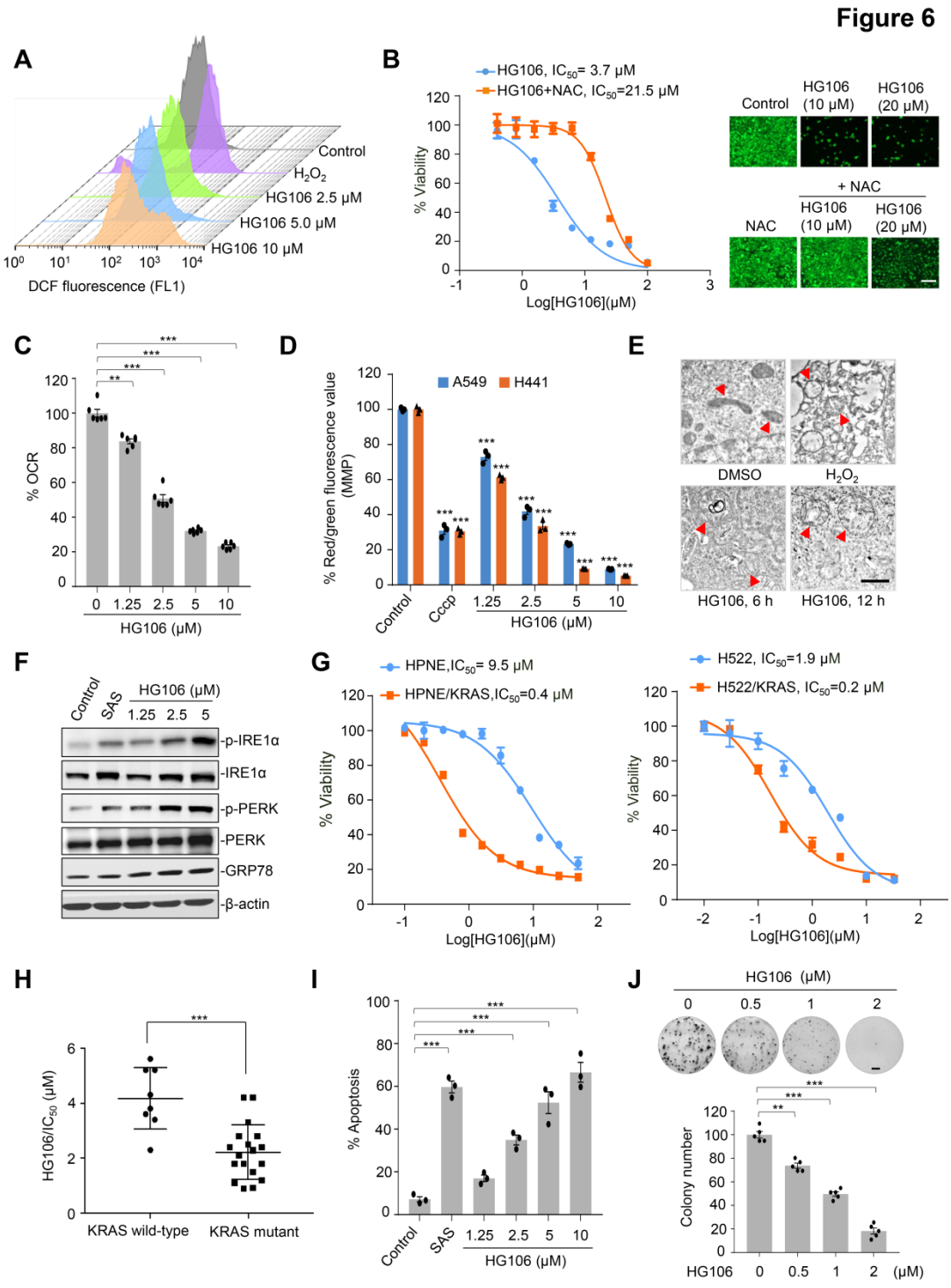

Figure 6. HG106 preferentially decreases viability of *KRAS*-mutant LUAD cells. (**A**) A 3D plot showing ROS production. A549 cells were treated with H_2O_2 for 1 h or different concentrations of HG106 for 6 h. (**B**) Effect of N-acetyl-cysteine (NAC, 10 mM) on HG106-induced cell death. A549 cells were treated with HG106 alone or in combination with NAC for 72 h, and cell viability was measured (*left*). The survival data for the HG106 group and the HG106+NAC group are normalized to the untreated control group and NAC alone group, respectively. Cell survival was also determined by Calcein-AM staining (*right*;

green, viable cells). Scale bars, 50 μm. (**C**) Basal mitochondrial oxygen consumption rate (OCR) changes in HG106-treated A549 cells. OCR values are normalized by sulphorhodamine staining. (**D**) Mitochondrial membrane potential (MMP) change in HG106-treated A549 cells. (**E**) Mitochondria morphology. Red arrowheads indicate mitochondria swelling. Scale bars, 0.5 μm. (**F**) HG106 activated ER stress-related markers. A549 cells were treated with HG106 and sulfasalazine (SAS, 1 mM) for 24 h. Immunoblots are contemporaneous and run in parallel from the same biological replicate. (**G**) Effect of HG106 on cell viability of KRAS isogenic cells. (**H**) HG106 displayed selective killing towards *KRAS*-mutant cancer cells. A panel of KRAS mutant (*n*=18) and KRAS wild-type (*n*=8) cancer cell lines (see Supplementary Table 9) were treated with HG106 for 72 h. *Dots*, IC_{50}s of each cell lines. (**I**) A549 cell apoptosis induced by HG106. (**J**) The effect of HG106 on A549 cell colony formation. Colony number was normalization to the control. Scale bars, 0.5 cm. All data are representative of at least 3 independent experiments, and shown as mean ± SD of biological triplicates. **P*<0.05, ***P*<0.01, ****P*<0.001 by one-way ANOVA with Tukey's multiple comparison test (C, D, I, and J), or by unpaired, 2-tailed Student's *t*-tests (H).

Figure 7

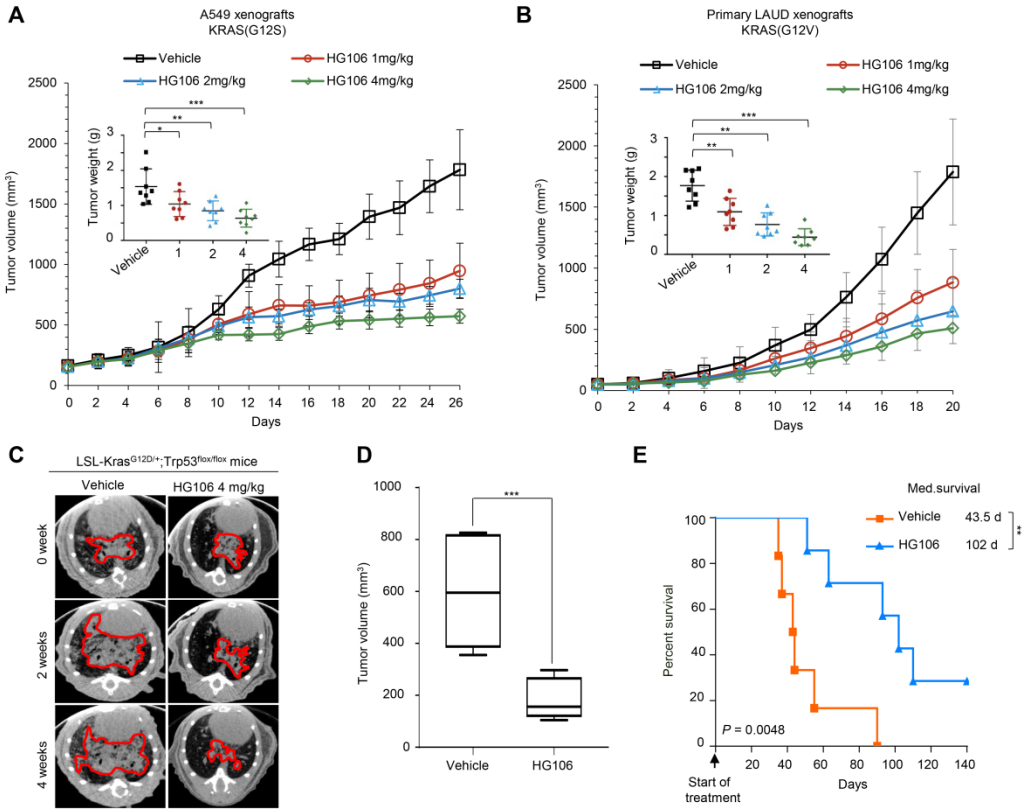

Figure 7. In vivo responses of *KRAS*-mutant LUAD to HG106. (**A**) A549 xenograft growth curve of (*n*=8). Mean weights of tumors at day 26 (*upper left*). (**B**) The growth curve of patient-derived xenografts (*n* = 8). Mean tumor weight at day 20 (*upper left*). The values are expressed as mean ± SEM. **P*<0.05, ***P*<0.01, ****P*<0.001 by one-way ANOVA with Tukey's multiple comparison test. (**C**) Representative tumor images of LSL-Kras$^{G12D/+}$;Trp53$^{flox/flox}$ (KP) mice. KP mice bearing established tumors were treated with HG106. Animals were scanned by micro-computed tomography during treatment. (**D**) The tumor volumes of KP mice (*n* = 6~7). The tumor volumes at the endpoint of indicated treatments are shown as box plots. Data are shown as mean ± SD. The horizontal lines representing the median; the bottom and top of the boxes represent the 25th and 75th percentiles, respectively; and the vertical bars representing the range of the data. ***P*<0.01 by unpaired, 2-tailed Student's *t*-tests. (**E**) Kaplan-Meier survival curves of KP mice (*n*=6~7). ***P*<0.01 by log-rank tests.

Figure 8

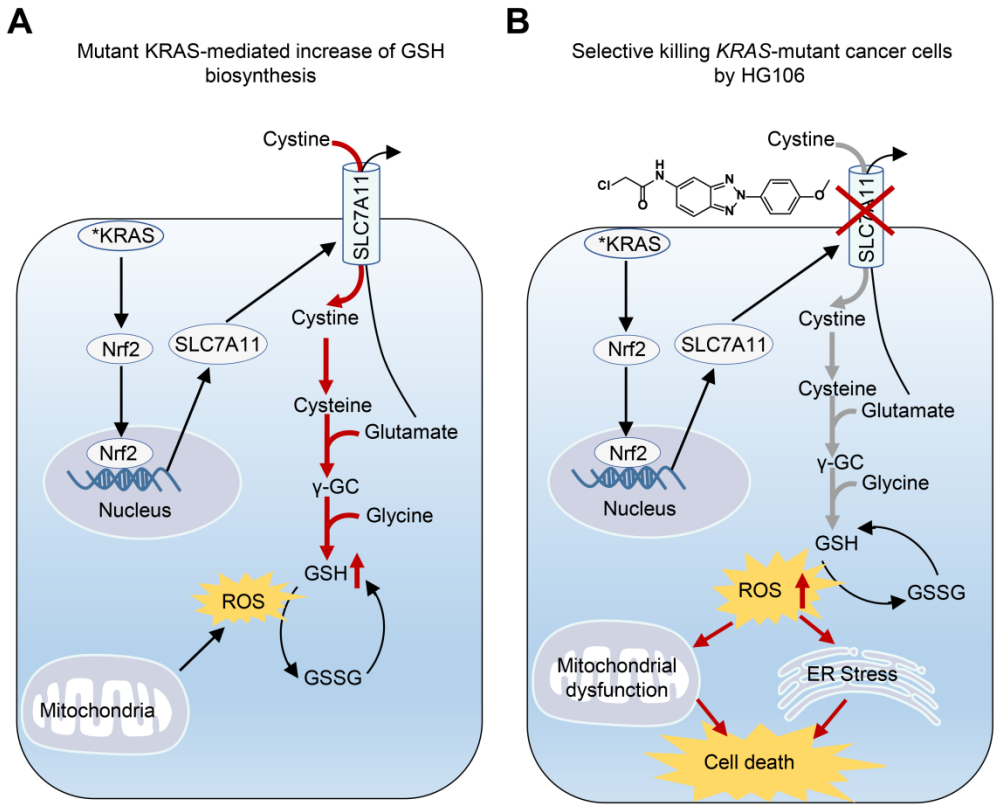

Figure 8. Schematic representation of *KRAS*-regulated glutathione metabolic reprogramming and the selective killing of *KRAS*-mutant cells by HG106. (**A**) Activated KRAS induces SLC7A11 overexpression through activating transcription factor Nrf2. As a consequence, SLC7A11 uptakes high level of cystine from the extracellular environment to generate more glutathione (GSH), which plays an important role in sustaining the oxidative balance in *KRAS*-mutant cells. Ultimately, *KRAS*-mutant cells are highly dependent on SLC7A11 mediated GSH biosynthesis. (**B**) When treated with HG106, a potent SLC7A11 inhibitor, cellular oxidant-antioxidant homeostasis is severely disrupted coupled with a significant mitochondrial dysfunction and endoplasmic reticulum stress, ultimately leading to massive cell death of *KRAS*-mutant cancers. Activated KRAS is indicated by an asterisk. Red arrows indicate pathway activation, and gray arrows indicate pathway inhibition.